Earth and Planetary Science Letters 450 (2016) 283–291

Contents lists available at ScienceDirect

Earth and Planetary Science Letters

www.elsevier.com/locate/epsl

Shallow earthquake inhibits unrest near Chiles–Cerro Negro volcanoes, Ecuador–Colombian border

Susanna K. Ebmeier [a,b,*], John R. Elliott [c,b], Jean-Mathieu Nocquet [d], Juliet Biggs [a], Patricia Mothes [e], Paúl Jarrín [e], Marco Yépez [e], Santiago Aguaiza [e], Paul Lundgren [f], Sergey V. Samsonov [g]

[a] COMET, School of Earth Sciences, University of Bristol, Queen's Road, Bristol, BS8 4JG, UK
[b] School of Earth and Environment, University of Leeds, LS2 9JT, UK [1]
[c] COMET, Department of Earth Sciences, University of Oxford, South Park Road, OX1 3AN, UK
[d] Geoazur, IRD, Université de Nice Sophia-Antipolis, Observatoire de la Côte d'Azur, CNRS, 250, Rue A. Einstein, 06560 Valbonne, France
[e] Instituto Geofisico – Escuela Politécnica Nacional, Ladrón de Guevara, E11-253, Aptdo. 2759 Quito, Ecuador
[f] Jet Propulsion Laboratory, M/S 300-233, 4800 Oak Grove Drive, Pasadena, CA 91109, USA
[g] Canada Centre for Mapping and Earth Observation, Natural Resources Canada, 560 Rochester Street, Ottawa, ON K1A 0E4, Canada

ARTICLE INFO

Article history:
Received 14 March 2016
Received in revised form 22 June 2016
Accepted 23 June 2016
Available online 9 July 2016
Editor: P. Shearer

Keywords:
volcanic hazard
earthquake
InSAR
GPS

ABSTRACT

Magma movement or reservoir pressurisation can drive swarms of low-magnitude volcano-tectonic earthquakes, as well as occasional larger earthquakes (>M5) on local tectonic faults. Earthquakes >M5 near volcanoes are challenging to interpret in terms of evolving volcanic hazard, but are often associated with eruptions, and in some cases enhance the ascent of magma. We present geodetic observations from the first episode of unrest known to have occurred near Chiles and Cerro Negro de Mayasquer volcanoes on the Ecuador–Colombian border. A swarm of volcano-tectonic seismicity in October 2014 culminated in a M_w 5.6 earthquake south of the volcanoes. Satellite radar data spanning this earthquake detect displacements that are consistent with dextral oblique slip on a reverse fault at depths of 1.4–3.4 km within a SSW–NNE trending fault zone that last ruptured in 1886. GPS station measurements capture ∼20 days of uplift before the earthquake, probably originating from a pressure source ∼10–15 km south of Volcán Chiles, at depths exceeding 13 km. After the M_w 5.6 earthquake, uplift ceased and the rate of seismicity began to decrease. Potential mechanisms for this decline in activity include a decrease in the rate of movement of magma into the shallow crust, possibly caused by the restriction of fluid pathways. Our observations demonstrate that an earthquake triggered during volcanic unrest can inhibit magmatic processes, and have implications for the hazard interpretation of the interactions between earthquakes and volcanoes.

© 2016 Elsevier B.V. All rights reserved.

1. Introduction

1.1. Earthquakes during volcanic unrest

Volcano Tectonic (VT) seismicity is common during volcanic unrest and eruption (e.g. Roman and Power, 2011) and usually consists of low-magnitude (<M4) earthquakes (e.g., Benoit and McNutt, 1996). Swarms of VT earthquakes have preceded many major explosive eruptions, with the highest rate of seismicity occurring at the onset of eruption (White and McCausland, 2016). More rarely, magmatic processes can trigger larger earthquakes on local tectonic faults. Earthquakes greater than magnitude 5 at volcanoes (listed in Supplementary Table 1) are associated with significant perturbations to subsurface stress fields (e.g., Mt St Helens 1980, Benoit and McNutt, 1996). This may involve static stress changes from the propagation of a dyke in the shallow crust (e.g., 2000 Miyakejima intrusion; Toda et al., 2002 or 1976 Krafla dyking episode; Passarelli et al., 2013) and most such examples take place during episodes of rifting with high rates of deformation (e.g., Wright et al., 2006; Biggs et al., 2009, 2013). Earthquakes >M5

* Corresponding author at: School of Earth and Environment, University of Leeds, LS2 9JT, UK.
E-mail addresses: s.k.ebmeier@leeds.ac.uk (S.K. Ebmeier), j.elliott@leeds.ac.uk (J.R. Elliott), nocquet@geoazur.unice.fr (J.-M. Nocquet), Juliet.biggs@bristol.ac.uk (J. Biggs), pmothes@igepn.edu.ec (P. Mothes), pjarrin@igepn.edu.ec (P. Jarrín), myepez@igepn.edu.ec (M. Yépez), saguaiza@igepn.edu.ec (S. Aguaiza), Paul.R.Lundgren@jpl.nasa.gov (P. Lundgren), sergey.samsonov@canada.ca (S.V. Samsonov).
[1] Present address.

http://dx.doi.org/10.1016/j.epsl.2016.06.046
0012-821X/© 2016 Elsevier B.V. All rights reserved.

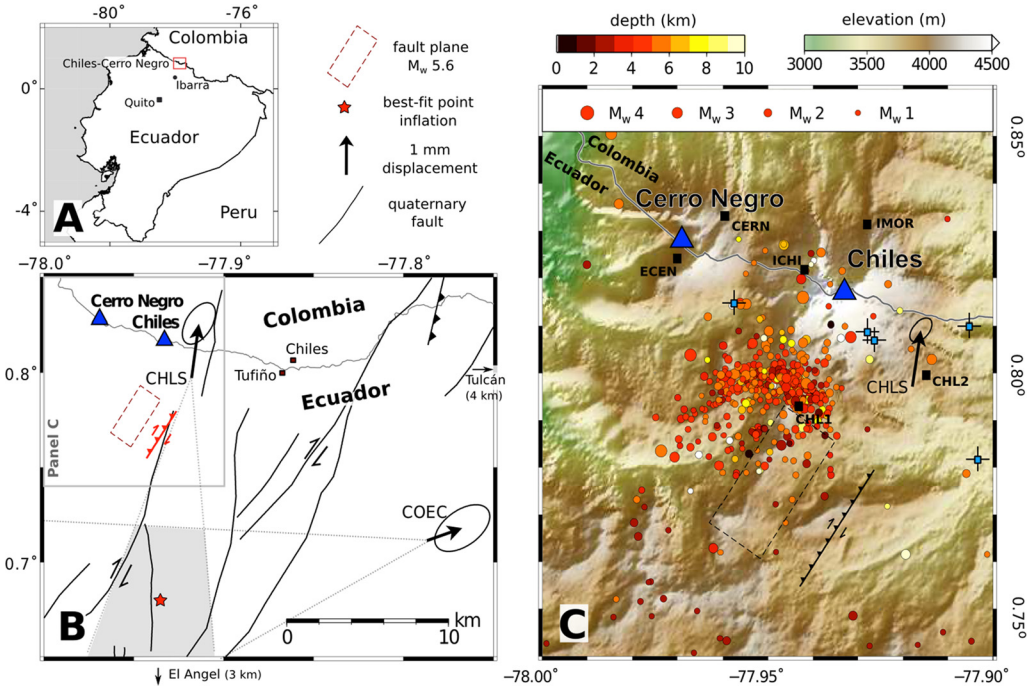

Fig. 1. A. Location of Chiles and Cerro Negro on the Ecuador–Colombian border. B. Map showing the locations of Chiles and Cerro Negro volcanoes (blue triangles), Quaternary faults (black), best-fit October 2014 point source pressurisation (red star) and uniform slip fault plane solution (red lines). Black arrows at GPS stations, CHLS and COEC, show horizontal displacements for the period of 01.10.2014–19.10.2014. Shaded grey area shows spatial locations that fit a point source to within GPS error. C. Instituto Geofisico catalogue earthquakes locations, depths and magnitudes from stations marked with black squares and stations names for 01.10.2014–19.10.2014 (e.g., Instituto Geofisico Escuela Nacional Politecnica, 2014; Ruiz et al., 2013). The locations of hot springs where geochemical monitoring is carried out by IG are indicated by blue squares on a cross hair. (For interpretation of the references to colour in this figure legend, the reader is referred to the web version of this article.)

have also been recorded during unrest at active volcanoes, where movement of magma or hydrothermal fluids is inferred from deformation, gas emission or seismicity (e.g., at Akutan and Peulik, Lu and Dzurisin, 2014; at Yellowstone, Wicks et al., 2006; near Sabancaya, Jay et al., 2015).

The largest group of earthquakes >M5 at volcanoes occur before, during or shortly after eruptions, and include some events with non-double couple focal mechanisms (Shuler et al., 2013). Earthquakes >M5 normally occur during explosive phases of eruption (e.g. at Chaitén in 2008, Wicks et al., 2011), although some have been attributed to post-eruptive stress readjustment (e.g., 1962 and 1983 at Miyakejima, Yokoyama, 2001) and caldera floor collapse (Riel et al., 2015).

VT swarms that include earthquakes >M5 may also precede eruption, as occurred before the 1999 eruption of Shishaldin (Moran et al., 2002). In some cases, such earthquakes may also play a more active role in triggering eruption. For example, a sequence of three M_w 5.2 events before the 1999 eruption of Cerro Negro, Nicaragua is thought to have reduced minimum principal stress and thus facilitated the ascent of magma (Diez et al., 2005).

The interpretation of earthquakes during volcanic unrest in terms of developing hazard is challenging. As the majority of reported >M5 earthquakes have been associated with major eruptions, the initial interpretation of such events would reasonably be one of increasing hazard. Here we use geodetic measurements during unrest near two volcanoes on the Ecuador–Colombian border, Chiles and Cerro Negro, to observe deformation before and after a M_w 5.6 earthquake and examine the relationship between magmatic intrusion and fault rupture.

2. Volcán Chiles and Cerro Negro de Mayasquer

Volcán Chiles and Cerro Negro de Mayasquer are stratovolcanoes that straddle the Ecuador–Colombian border and have had no recorded historical eruptions (Fig. 1A–B). Volcán Chiles last erupted about 160,000 yr ago whilst andesitic and dacitic lava flows in Cerro Negro caldera are possibly of Holocene age. The most recent erupted material to have been dated from either volcano comes from a debris avalanche at Cerro Negro and is at least 3000 years old (Cortés and Calvache, 1997). An active geothermal system extends to the south of Chiles, manifesting in numerous hot springs (Fig. 1C, Instituto Geofisico Escuela Nacional Politecnica, 2014, No. 27). Their lack of historical activity and remote location on an international border have meant that until 2013, both volcanoes were monitored with minimal instrumentation, and were classified as 'potentially active' by the Instituto Geofisico ('IG', Escuela Politécnica Nacional) and 'active but stable' by the Pasto Volcano Observatory, Servicio Geológico Colombiano ('SGC'). Low-level seismicity (<10 VT and low frequency events per month) was reported at Chiles–Cerro Negro from 1991 onwards, when the IG installed a single seismometer, and has been attributed to an active hydrothermal system (Ruiz et al., 2013).

In October 2013, a seismic swarm consisting of >1000 recorded events per day occurred 2–6 km south of Chiles. Two further VT swarms took place in February–May 2014 and September–December 2014. The SGC changed the volcanoes' alert level from green ('active but stable') to yellow ('changes to the volcano's activity') in April 2014, in response to the increase in the rate and magnitude of VT earthquakes (SGC, Boletín Mensual No. 04-2014). The 2014 VT swarms had increasing duration and event rate, but were separated by periods of low-level seismicity of the order of 10s to 100s of events per day. The majority of the earthquakes had depths of between 2 and 5 km, were < M4, and concentrated in a ~25 km^2 area to the southwest of Chiles (Fig. 1C). All three swarms occurred in approximately the same location, and larger events (M 3–4) occurred later, rather than at the beginning, of each sequence. These 'swarm-like' characteristics are more likely to be associated with pore-fluid pressure changes than with cascading

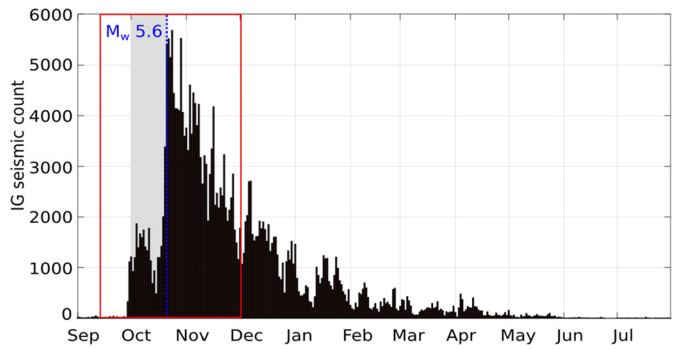

Fig. 2. Seismic count from Instituto Geofisico catalogue at Chiles–Cerro Negro between September 2014 and July 2015 (some initial counts, including automatically identified earthquakes that had not yet been quality-controlled, were generally higher and found ∼8000 events per day on the 20th October 2014, e.g., Instituto Geofisico Escuela Nacional Politecnica, 2014, No. 26). Catalogue earthquakes were located using data from eight seismometers, mostly to the north of the volcanoes, and including those shown on Fig. 1C plus ICAN (−77.9505, 0.864333) and IPAN (−77.8805, 0.850667). The grey shaded box shows the period of uplift detected by the GPS and shown in Fig. 3.

elastic failures (Vidale et al., 2006) and are similar in this respect to VT seismicity at many other volcanoes (White and McCausland, 2016). The Chiles–Cerro Negro seismic swarms were dominated by high frequency events thought to be associated with brittle failure, but there were also low frequency components to some waveforms later in the unrest that could indicate fluid movement (Ruiz et al., 2013; Salvage, 2015).

In October 2014, there were >5000 small earthquakes detected per day (Fig. 2), including some long period events (e.g., Chouet and Matoza, 2013). At this time, some of the larger earthquakes were felt in Tulcán and Tufiño in Ecuador (Instituto Geofisico Escuela Nacional Politecnica, 2014, No. 23), and by residents of the Resguardos Indígenas del Municipio de Cumbal in Colombia (SGC, Boletín Mensual No. 10-2014). On the 20th October at 19:33 UTC a M_w 5.6 earthquake caused damage to buildings in villages near Volcán Chiles (Instituto Geofisico Escuela Nacional Politecnica, 2014, No. 23). The escalation in the rate and increase in maximum magnitude of the seismic swarms, as well as the M_w 5.6 earthquake were interpreted as evidence for the ascent of magma. Both the IG and the SGC changed their assessment of the volcano activity level from yellow to orange, meaning that an eruption was expected within days to weeks. The number of VT earthquakes per day reached their maximum on the 24th October, four days after the M_w 5.6 earthquake, and presumably encompassing aftershocks from the larger event. After this, the number of earthquakes per day started to decline and had gradually returned to background levels by May 2015 (Fig. 2), suggesting a cessation of magma ascent (e.g., Moran et al., 2011). There were no changes considered significant relative to background levels in the pH or temperature of hot springs monitored by the IG (locations marked on Fig. 1C), or in fumerolic activity on the western side of Cerro Negro's crater (Instituto Geofisico Escuela Nacional Politecnica, 2014, No. 27). In response to the decrease in seismicity, GPS deformation and InSAR measurements of the M_w 5.6 earthquake, the volcanic alert level was returned from orange ('eruption anticipated within days to weeks') to yellow (SGC: 'changes to the volcano's activity' and IG: 'potentially active') by both the SGC and IG on 26th November 2014.

3. Data and methods

3.1. GPS data 1st–19th October 2014

We analysed GPS data from the IG tectonic network station COEC, located ∼15 km to the southeast of the volcanoes and from

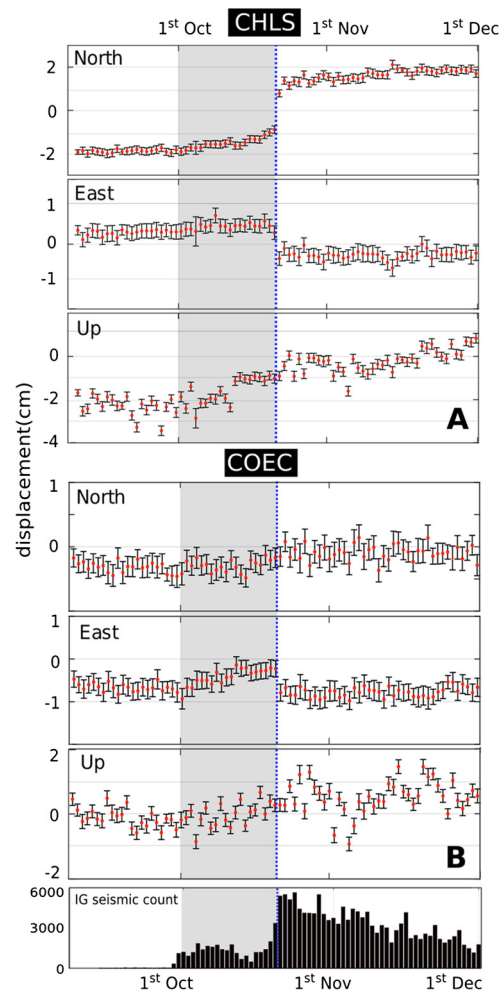

Fig. 3. GPS time series displacements (10.09.2014–1.12.2014) for stations CHLS (installed 10.05.2014) and COEC. Error bars show 1-sigma errors for the daily solutions. The date of the M_w 5.6 earthquake, 20th October, is indicated by a dashed line and the shaded grey box indicates the approximate period of uplift also shown on Fig. 2. The seismic count from the Instituto Geofisico catalogue for the same time period is shown in the lower panel.

a second site, CHLS, installed ∼2 km from Volcán Chiles on 10 May 2014 (Fig. 1). We use GAMIT 10.6 (King and Bock, 1999) to process the GPS data from CHLS and COEC with an Ecuador wide continuous GPS network (Mothes et al., 2013). Each daily solution is first transformed into the International Terrestrial Reference Frame ITRF2008 (Altamimi et al., 2011) using a 7-parameter transformation. Final time series (Fig. 3) are expressed in a north Andean Sliver reference frame by removing the trend predicted by the Euler pole proposed by Nocquet et al. (2014).

CHLS and COEC stations recorded displacements between the 1st and 19th October 2014 indicative of pressurisation to the south of the volcanoes. TerraSAR-X interferograms that spanned this time period do not extend far enough south to capture this signal (Supplementary Fig. 2). We therefore used the 3D displacements from both GPS stations to find the horizontal location and depth of the pressurisation responsible for these displacements. Data from both GPS stations are noisy (especially COEC) and are not in themselves sufficient to constrain a unique source geometry. We therefore used a simple point source, elastic half space model to investigate the potential range of depths for a pressurising source. We consider this a more appropriate interpretation of the data than a model with realistic rheology, topography and source geometry but that requires more degrees of freedom. As the variance in horizontal GPS displacements is much lower than for the ver-

tical displacements, we first used these to find the best-fit latitude and longitude of a point pressurisation source and to identify the horizontal region within which it is likely to be located. We then used a grid search approach, minimising misfit between the predicted and observed GPS displacements, to find the regions of the depth-volume change parameter space within which the early October source could be located (Supplementary Fig. 1). We consider solutions with a root mean square error less than 1.5 mm (150% of the minimum value, and within the range of standard deviations in GPS daily solutions of 1–3 mm) to be a reasonable fit to the GPS data.

3.2. InSAR analysis of 20th October M_w 5.6 earthquake

We used Interferometric Synthetic Aperture Radar (InSAR) to measure displacements during the October 2014 swarm. Deformation was captured by four independent interferograms (Supplementary Fig. 2) from three satellite instruments: TerraSAR-X (18.10.2014–27.11.2014 descending), CosmoSkymed (28.03.2014–30.10.2014 descending and 14.03.2014–30.10.2014 ascending) and RADARSAT-2 (17.05.2014–01.11.2014 descending). We are confident that the displacements captured in these interferograms primarily represent displacements associated with the M_w 5.6 EQ because two earlier TerraSAR-X images (spanning 03.03.2014–28.05.2014 and 28.05.2014–18.10.2014) show no deformation above a magnitude of ∼1 cm, despite continued low-magnitude seismicity. Interferograms were constructed using ISCE (Rosen et al., 2011) and GAMMA software (Wegmuller et al., 1998), and topographic contributions to interferogram phase were corrected using the 30 m SRTM DEM (Rosen et al., 2001). Unwrapping was carried out using the Snaphu algorithm (Chen and Zebker, 2002).

All four interferograms were downsampled using nested uniform sampling (1800 m pixels) with a higher sampling density (400 m pixels) over the regions of high magnitude deformation (Supplementary Fig. 3). We model the line-of-sight displacements as dislocations from uniform slip on a rectangular fault plane in an elastic half-space (Okada, 1985) and take $\lambda = \mu = 3 \times 10^{10}$ Pa as the Lamé parameters. We jointly invert the downsampled line-of-sight displacements from all four interferograms for uniform slip on a single fault. First, to constrain the fault geometry, we invert all four interferograms and solve for slip, strike, dip, rake, surface centre location, length, and top and bottom depths. We estimate errors on these parameters by performing a Monte Carlo analysis where the inversion was performed 250 times on data sets perturbed by randomly generated synthetic noise with the same variance and e-folding distances (Hanssen, 2001) as the data (Supplementary Table 2, Supplementary Fig. 4). We next refine our model by solving for distributed slip on the best-fit fault plane. The data are inverted using a non-negative least squares algorithm and Laplacian smoothing (e.g., Funning et al., 2005). We extend the length and height of the fault plane and divide into patches of side length 0.5 km, solving linearly for variable slip and rake on each patch, which has a fixed geometry (Funning et al., 2005).

3.3. Stress change modelling

Faults can be brought closer to failure by an increase in Coulomb stress, $\Delta\sigma_C = \Delta\tau - \mu'\Delta\sigma_N$, either through (1) an decrease in normal stress, $\Delta\sigma_N$ ('unclamping'), (2) an increase in shear stress, $\Delta\tau$, and/or (3) a decrease in the effective coefficient of friction (μ') on the fault plane (Stein, 1999; Jolly and McNutt, 1999).

We investigate the stress and strain changes generated by both point pressurisation sources that match the early October GPS displacements and the M_w 5.6 earthquake using the United States Geological Survey code Coulomb 3.1 (Lin and Stein, 2004). As the location of the early October pressurisation is poorly constrained by the GPS data, we investigate the stress changes caused by a range of different point source locations at intervals of ∼0.02° within the ranges of 0.64°N–0.74°N latitude and 78.0°W–77.9°W longitude. For each horizontal location we also test a range of depths (10, 15, 20, 25 km) and corresponding volume changes (Supplementary Fig. 1), assuming $\mu' = 0.4$. We estimate Coulomb stress changes for each case on our preferred fault plane for the M_w 5.6 earthquake.

We investigate whether uncertainties in the estimated fault strike of ±2°, (1σ errors, Supplementary Fig. 4), and corresponding variations in fault position and geometry, have an impact on the Coulomb stress changes for a given point pressurisation location, depth and volume, but find that differences are negligible. The differences in strains predicted by the uniform and distributed slip solutions are also negligible.

4. Results

Between the 1st and 19th October 2014, CHLS was displaced northward (9 ± 2 mm) and upwards (15 ± 9 mm), coincident in time with eastward displacement (6 ± 3 mm) at COEC (Fig. 3), all relative to the North Andean Sliver (Nocquet et al., 2014). Other components of displacement over this time were lower than average uncertainties in daily solutions of ∼2–3 mm horizontal displacement and ∼8–9 mm vertical displacement (95% confidence level). No deformation was reported from either GPS site before the 1st October 2014 (although CHLS was installed only on 10th May 2014). The TerraSAR-X interferograms that extended from 28th May to 18th October (144 days) also show no deformation at either volcano or in the location of the VT swarm (but did not extend as far south as our preferred early October inflation source location, Fig. 1). The displacements recorded at the GPS stations were of similar magnitude (CHLS 1st–19th October is equivalent to ∼13 mm in TSX line of sight) to the variance in interferogram phase (∼10 mm) and are not apparent in the coherent patches of the interferograms. After the M_w 5.6 earthquake on 20th Oct, displacements appeared to cease at both GPS stations. Average displacement rates over the twenty days afterwards were lower than average uncertainties in daily solutions, except for the northward displacement of CHLS, which may have continued for a few days at a much lower rate than before the earthquake.

The trends of northward and vertical displacement at CHLS between the ∼1st and 19th October are well above the uncertainties in daily solutions, and show that the source certainly lies to the south of the GPS station (Fig. 1B), rather than at Volcán Chiles itself or at the densest part of the seismic swarm (Fig. 1C). The direction of movement of COEC is also clearly eastward until the M_w 5.6 earthquake on 20th October, when it reversed to westward. This change in direction at COEC but not CHLS means that GPS displacements are unlikely to be related purely to slip on the fault that ruptured during the M_w 5.6 earthquake. Deformation can also not be attributed to the cumulative slip of the thousands of < M4 VT earthquakes during 1–19th October: the earthquakes are distributed over a broad area of ∼10 km^2 west of the GPS stations and have a cumulative magnitude of only ∼M4.

Our analysis shows that GPS displacements are matched by pressurisation at ∼(−77.95°W, 0.67°N) at depths exceeding 13 km and less than 25 km (Fig. 1B, Supplementary Fig. 1). The horizontal location of such a pressure source could vary over ∼5 km while still fitting the GPS data to within 3 mm. We do not have good constraints on volume change because we do not know reservoir and magma compressibility or the temperature profile of the crust (and therefore viscoelasticity). Alternative source geometries such as an ellipsoid (Yang et al., 1988, 8 free parameters) or sill (Okada, 1985, 8 free parameters) would also need to be located

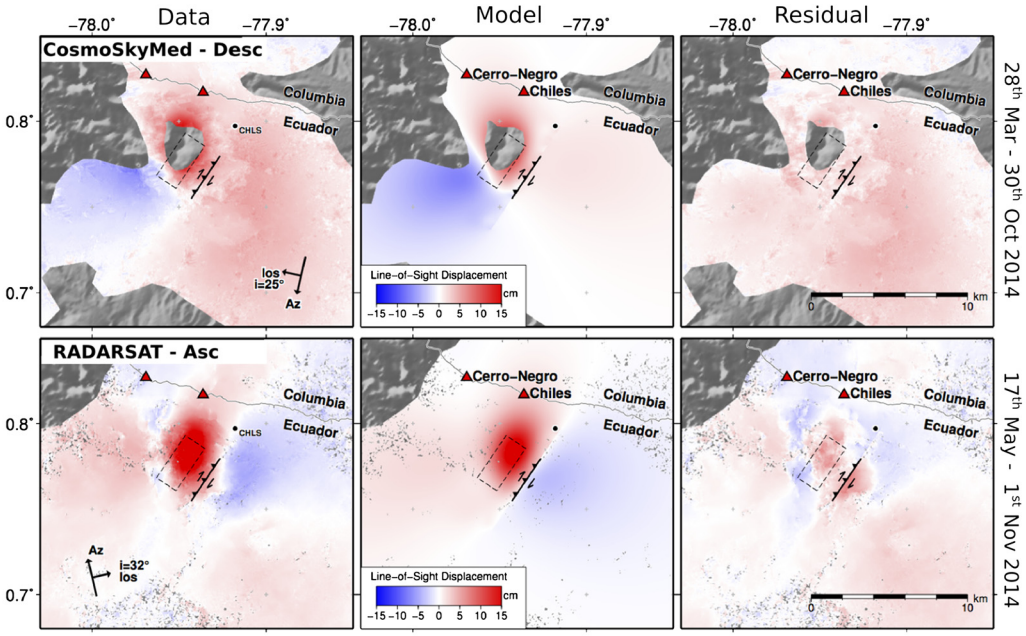

Fig. 4. Examples of line of sight InSAR displacements from descending CosmoSkymed (28.03.2014–30.10.2014) and ascending RADARSAT-2 data (17.05.2014–1.11.2014). Line of sight (los) azimuth direction and incidence angle are indicated on individual panels. Model panels show the predicted line of sight displacements for our preferred uniform slip solution (strike = 213 ± 2°, dip = 50 ± 1.6° and rake = 151 ± 2.4°, slip = 1.2 m). Line-of-sight displacements (red–blue colour scale) are overlaid onto hill shaded SRTM topography. (For interpretation of the references to colour in this figure legend, the reader is referred to the web version of this article.)

in the mid-crust (>10 km) to satisfy the low magnitude of upward GPS displacements (15 ± 5 mm and 6 ± 4 mm at CHLS and COEC, respectively). The GPS displacements could potentially also be produced by the opening of a dyke, though this would have to have been deep enough that opening could be accommodated without seismicity. The only cluster of earthquake locations during 1st–19th October was to the east of CHLS (Fig. 1C), mostly between 2 and 6 km depth. A dyke intrusion in the shallow crust in this region could not have produced the observed GPS displacements, and would also have caused a measureable deformation signal in the interferograms, which were coherent in this area and showed no displacements up to 18th October 2014.

The InSAR displacements spanning the 20th October EQ are well matched by 1.2 m of slip on a fault of strike = 213 ± 2°, dip = 50 ± 1.6°, rake = 151 ± 2.4°, length = 3.4 km, giving a moment equivalent to an earthquake of M_w 5.6 (Fig. 4). The modelled rupture was shallow, between depths of 3.4 and 1.4 km, and the southern edge of the fault rupture lies >6 km north and at least 10 km shallower than the early October source. Comparison of the root mean squared misfit for inversion with slip fixed at intervals show that misfit decreases with increasing slip up to a value of 0.8 m, after which misfits level off. However, the model fit to the maximum co-seismic displacements, over the footwall of the fault, is best for slip of 1.2 m. Our preferred fault plane solution implies a relatively high stress drop of 14 MPa, but this could vary by ±3 MPa (Supplementary Fig. 4), and could therefore be as low as 10 MPa. The auxiliary plane solution (dipping to southeast) does not provide as good a match to the data as our preferred solution (e.g. RMS of residuals was 0.2 cm higher for CosmoSkyMed and TerraSAR-X interferograms).

Our variable slip and rake solution for fixed geometry (Fig. 5A) demonstrates that the slip at the south-western end of the fault was almost pure right-lateral, and that the reverse component of slip became more significant in the northeast. Our InSAR derived focal mechanism is in reasonable agreement with the IPGP seismological analysis (Vallée et al., 2011) of the waveform (M_w 5.7 and strike 224°, dip 62° and rake 163°), although fault locations differ

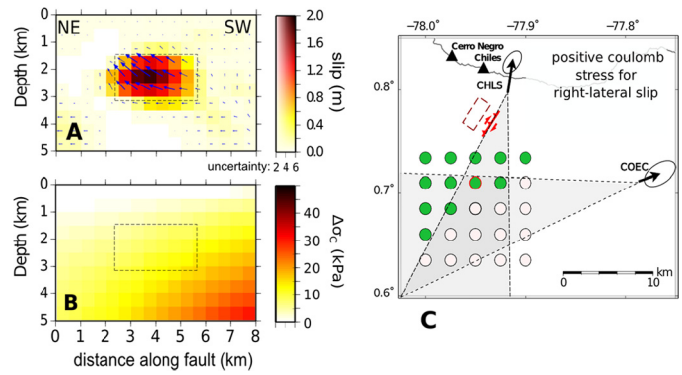

Fig. 5. A. Distributed slip solution for slip on a fault plane with the geometry of our uniform slip solution, where slip magnitude and uncertainty is shown by the colour scale and rake by blue arrows. B. Example of Coulomb stress changes for right lateral slip on the plane defined by our uniform slip solution. The dashed box marks the edge of the region of slip and the location of the early October pressurising source is marked with a red outline on part C. C. Source locations for which Coulomb stress change for right-lateral slip on the southwestern corner of the fault plane is positive are indicated by green circles (white circles indicate that Coulomb stress changes are negative). (For interpretation of the references to colour in this figure legend, the reader is referred to the web version of this article.)

by ∼30 km, which is within the range of error (10–30 km) expected for global seismological locations (e.g., Elliott et al., 2010).

Whether or not the modelled early October pressurisation would have brought this fault closer to failure depends on its location: some acceptable source locations increase Coulomb stress ($\Delta\sigma_C$) on the fault plane, while others lower it. Normal stress change across almost the whole fault plane is negative (1–10 kPa, unclamping) for pressurisation at locations within the bounds of models constrained by GPS measurement, but shear stresses on different parts of the fault vary in magnitude and sign (∼5–5 kPa). At the part of the fault plane closest to the magmatic intrusion, slip is close to pure right-lateral, so we estimate Coulomb stress change for right-lateral motion and find that $\Delta\sigma_C$ is positive for early October pressurisation sources located at the northern side of the range required by GPS measurements (10–30 kPa on southwestern

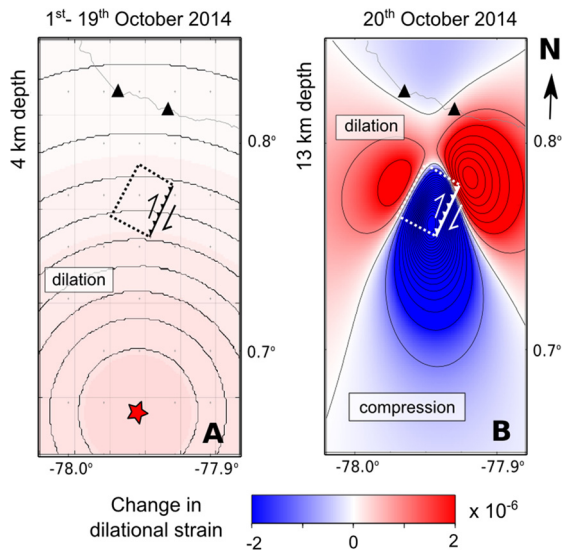

Fig. 6. A. Change in dilational strain at 4 km depth for the pressurisation of a point source at our best-fit location and at 13 km depth. B. Change in dilational strain caused by the 20th October M_w 5.6 earthquake at 13 km depth. Blue shows compression and red indicates dilation. (For interpretation of the references to colour in this figure legend, the reader is referred to the web version of this article.)

corner of the fault, e.g., Fig. 5B–C). A more complex source geometry (e.g. an opening sill or pressurising prolate ellipsoid) could potentially generate quite different stress fields (see Albino and Sigmundsson, 2014), but these would also be sensitive to position and trade-offs between depth and volume change or opening. It is therefore possible, but not certain, that the static stress changes contributed to triggering the M_w 5.6 earthquake. The earthquake itself caused an increase in dilational strain west and east of the fault plane, but resulted in a lobe of negative dilational strain (volumetric compression) in the upper crust in the vicinity of the early October pressurisation (Fig. 6B).

For pressurisation near our best-fit location, we estimate that $\Delta\sigma_N$ and $\Delta\tau$ on the fault are of the same order of magnitude, making $\Delta\sigma_C$ very sensitive to small changes in the effective coefficient of friction, μ', and therefore pore pressure. Pressurisation of the early October source also caused dilation in the surrounding crust (Fig. 6A) and may have caused an increase to the flow of fluids into the hydrothermal system. Elevated pore fluid pressure may both have reduced the effective friction on the El Angel zone fault, and contributed to the increase in the rate of VT seismicity before the 20th October. Our estimations of Coulomb stress changes are within the range thought to cause variations in rates of seismicity due to hydrological loading (2–4 kPa; Bettinelli et al., 2008) and in rates of volcanic tremor due to fluid tides (15 kPa; Rubinstein et al., 2008).

5. Discussion

5.1. Mid-crustal magmatic source

GPS displacements from 1st–19th October 2014 are best matched by a pressurising source within a ∼5 km radius of (−77.95°, 0.67°) at depths of >13 km. The source location is constrained by only two GPS stations, so the uncertainty in its location is high, but we are confident that 1) it lies to the south of CHLS and west of COEC and 2) that it is at least at mid-crustal depths. Because the GPS data indicate a pressurisation at mid-crustal depths, we interpret it as evidence for magma reservoir pressurisation, rather than a hydrothermal process. The volume, or even lateral extent, of the magma reservoir associated with the Chiles–Cerro Negro unrest is, however, unclear.

There has been no prior indication of an eruption at the above modelled early October pressure source location. The surface of this area is covered with old (>10,000 yr), poorly studied volcanic deposits and to our knowledge has not been the site of historical seismic swarms. After Chiles–Cerro Negro (∼15 km north of the early October pressure source), the next nearest Holocene volcanoes are >40 km away (Chachimbiro, ∼45 km WSW; Imbabura ∼50 km SW and Soche, ∼45 km, ESE). However, deformation located tens of kilometres away from the nearest known volcanic centre is a common observation in regional InSAR surveys (e.g., Pritchard and Simons, 2004; Biggs et al., 2011; Lundgren et al., 2015) and distal VT seismicity up to 15 km away from the associated volcano is also a common observation at the onset of both eruptions and intrusions (White and McCausland, 2016).

5.2. Origin of the M_w 5.6 earthquake

The M_w 5.6 earthquake occurred on a fault aligned with a SSW–NNE trending system in an extension of the Romeral fault in Colombia (e.g., Ego et al., 1996). Two large earthquakes occurred on this fault system in August 1868 near the towns of El Angel (at ∼−77.9°W, 0.7°N) and Ibarra (at ∼−78.45°W, 0.36°N), with magnitudes in the range 6.4–6.8 and 7.1–7.7 respectively, as estimated from intensity data (Beauval et al., 2010). The regional strain field is dominated by the subduction of the Nazca plate at a rate of ∼46 mm/yr (Nocquet et al., 2014) and deformation within the North Andean Sliver. The direction of maximum compressive stress derived from focal mechanism inversion for historical earthquakes <60 km depth in the Romeral fault area is ∼076°N (Ego et al., 1996), which is in reasonable agreement with a horizontal direction of displacement of 052°N from the 2014 M_w 5.6 earthquake. The M_w 5.6 earthquake was on an active fault that had potentially been locked at least since 1868, and is likely to have been stressed before the unrest in 2014.

It is unlikely that the M_w 5.6 earthquake occurred during the 2014 Chiles–Cerro Negro swarm by coincidence. Between 1980 and the end of 2015 there were only 9 earthquakes >M5 at depths <50 km within a 100 kilometres radius of Chiles–Cerro Negro volcanoes (Supplementary Table 2). The M_w 5.6 earthquake was preceded by an acceleration in the rate of seismicity (Salvage, 2015), suggesting that the same underlying process drove both the VT swarm and triggered the M_w 5.6 earthquake.

5.3. Elevated pore-fluid pressure in the shallow crust

Our Coulomb stress calculations show that static stress changes from magma movement in October 2014 could potentially have brought the El Angel fault closer to failure, but the impact of mid-crustal magmatic activity on the hydrothermal system that feeds the multiple hot springs south of Chiles and Cerro Negro may have been equally or more important. The swarm-like characteristics of seismicity at Chiles–Cerro Negro are indicative of elevated pore-fluid pressure (e.g., Vidale et al., 2006), which could be either due to heating of groundwater, or the ascent of magmatic fluids (Jolly and McNutt, 1999). The deep magmatic intrusion in early October caused dilation (Fig. 6), which may have increased the flow of magmatic fluids into the hydrothermal system, elevating pore fluid pressure. Both the majority of the VT events during the 2013–2014 unrest, and the fault that ruptured in the M_w 5.6 earthquake lie at depths (2–6 km). This is consistent with a shallow hydrothermal system to which background seismicity at Chiles and Cerro Negro has been attributed (Ruiz et al., 2013; Cortés and Calvache, 1997).

5.4. The impact of the M 5.6 earthquake: suppression of unrest

The 20th October M_w 5.6 earthquake coincided with the cessation of the uplift seen in GPS measurements, and preceded the

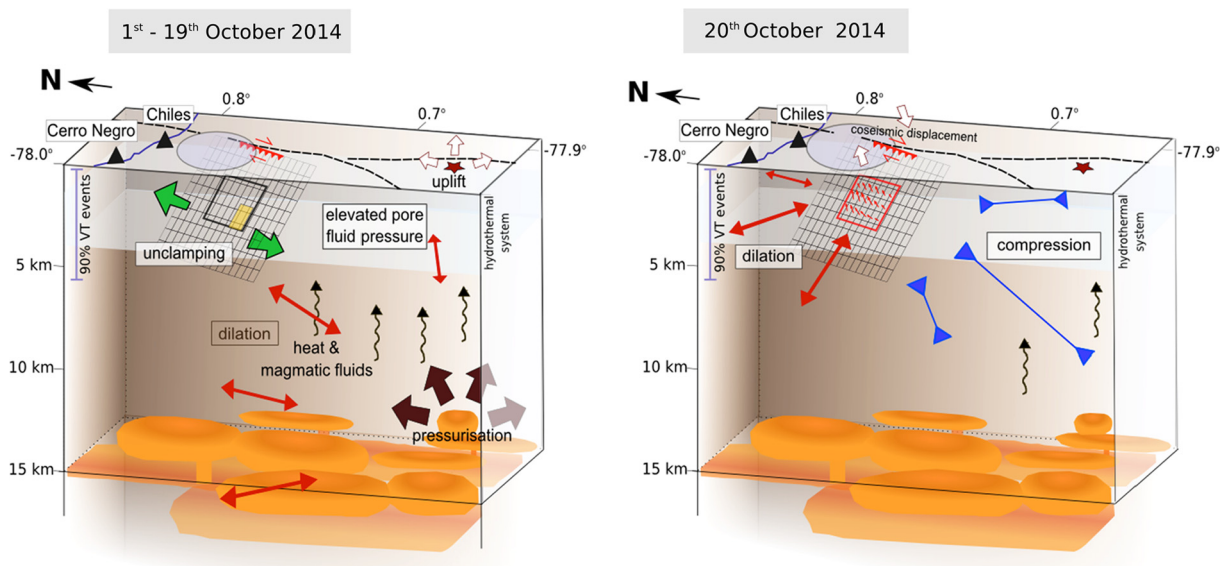

Fig. 7. Schematic representation of processes at Chiles–Cerro Negro pre-earthquake 01.10.2014–19.10.2014 and the M_w 5.6 earthquake on 20.10.2014. Blue ellipses indicate the distribution of 90% of VT hypocentres. (For interpretation of the references to colour in this figure legend, the reader is referred to the web version of this article.)

start of a gradual decrease in number of seismic events per day after 24th October (Figs. 2 and 3). IG catalogue earthquake locations suggest that more earthquakes, with higher average magnitudes, occurred closer to the northern end of the M_w 5.6 fault plane during the four days after the 20th October than the four days before (Supplementary Fig. 6). The rate of decay in seismic event count after this time is likely to encompass contributions from an aftershock sequence from the M_w 5.6 earthquake, as well as a more gradual decrease in VT seismicity from pre-20th October levels. Since October 2015, both GPS stations and repeated satellite radar measurements of the region around Chiles and Cerro Negro show no evidence of further deformation.

A possible explanation is that the M_w 5.6 earthquake affected the subsurface stress field so that it changed how magmatic processes were accommodated (Fig. 7). For example, a transition from an earlier upward migration into the elastic crust, to a deeper, lateral movement of magma would diminish any measurable deformation. Strain changes caused by the earthquake (Fig. 6B) may also have brought about a change to the pattern of fluid flow, potentially restricting the migration of fluids into the hydrothermal system; increasing the flow of hydrothermal fluids out and therefore decreasing pore-fluid pressure. Such shifts in deformation patterns have been recorded during periods of elevated seismicity at both Long Valley (1997–1998) and Yellowstone calderas (1985, 1995) and attributed to changes to the flow of hydrothermal and magmatic fluids caused by tectonic processes (e.g., Hill, 2006; Wicks et al., 2006).

5.5. Negative feedback on magmatic processes

Large earthquakes have been shown to trigger volcanic unrest (e.g., Pritchard et al., 2013; Takada and Fukushima, 2013; Battaglia et al., 2012) and eruption (Linde and Sacks, 1998) by causing static and dynamic stress changes (Manga and Brodsky, 2006). Some detailed case studies have demonstrated positive feedback, where moderate earthquakes and faulting enhance the magmatic processes thought to have triggered them. This can occur during the onset of eruption, for example during the 1999 eruption of Cerro Negro in Nicaragua (Diez et al., 2005) or during cycles of trapdoor faulting and sill growth at Sierra Negra in the Galapagos (Jónsson, 2009). During the early stages of dyke intrusion near Lake Natron, slip on a normal fault unclamped the source region of a vertically propagating dyke, but increased clamping at shallower depths. In this case, stresses at the dyke tip were sufficient to overcome clamping effects and allow the vertical propagation of the dyke, so that the net impact of the fault slip on magma ascent was positive (Biggs et al., 2013).

Examples of equivalent negative feedback, where earthquakes triggered during volcanic unrest inhibit an underlying magmatic process, appear to be rarer (or at least less frequently reported). However, a recent study, Maccaferri et al. (2016), used mechanical modelling to demonstrate that stress transfer from a M 6.5 earthquake triggered at the tip of a propagating dyke at Miyakejima in 2000 was the primary cause for its arrest. Interaction with faulting has also been implicated as an important factor in the arrest of a dyke at Harrat Lunayyir in 2009 (Xu et al., 2016), and is expected to be a widespread process.

Although many earthquakes >M5 have been reported during volcanic unrest (Supplementary Table 1), their relationship to the underlying magmatic process is often unclear (e.g. during VT swarms at Akutan and Peulik; Lu and Dzurisin, 2014). Our observations from near Chiles–Cerro Negro are unusual in that they document a turning point in both VT seismicity and GPS displacement that coincide with a triggered tectonic earthquake. A similar event may have taken place at Iwatesan volcano (Japan) in 1998, when a M 6.1 earthquake occurred during a VT swarm, and was attributed to stress changes from pressurisation ∼12 km west of the volcano's summit (Nishimura et al., 2001). Although seismicity and deformation after the earthquake are not documented, Nishimura et al. note that "the volcanic activity came to be calm after the occurrence of the M 6.1 earthquake," which implies that, as at Chiles–Cerro Negro, the earthquake may have inhibited the underlying process that had been driving unrest.

Earthquakes initiating an escalation in magmatic activity have been more frequently reported than those causing a diminishment. In particular, many examples of larger earthquakes occurring during VT swarms immediately before eruption mean that larger earthquakes are necessarily interpreted as indicating elevated volcanic hazard. Our observations at Chiles–Cerro Negro demonstrate that in some cases this interpretation results in 'false positives' where no escalation to eruption takes place, and furthermore that such earthquakes may act to inhibit magma movement.

6. Conclusions

The first measured unrest near Chiles–Cerro Negro volcanoes took place in 2013–2014 and consisted of three episodes of VT seismicity and a brief period of uplift in October 2014. After a M_w 5.6 earthquake on 20th October 2014, uplift ceased and seismicity began to fall. Our interpretation of the sequence of events at Chiles–Cerro Negro based on our GPS and InSAR measurements from October 2014 is as follows:

- The pressurisation of a mid-crustal magma reservoir (>13 km depth, ∼15 km south of Volcán Chiles) caused displacements at two GPS stations 1st–19th October 2014. This pressurisation caused dilation, which may have contributed to increased fluid flow in the hydrothermal system and the observed increase in the rate of VT seismicity.
- On the 20th October a M_w 5.6 earthquake occurred on a shallow fault in the El Angel fault zone, probably triggered by elevated pore fluid pressure, possibly with some contribution from static stress changes caused by the deep pressurisation.
- The earthquake caused strain changes in the subsurface that coincided with (1) the cessation of GPS displacements, (2) a gradual decrease in the rates of VT seismicity. This may have been due to transition in fluid flow and mode of magma storage.

Our observations at Chiles–Cerro Negro are important because they demonstrate that an earthquake triggered during volcanic unrest can inhibit, rather than enhance, the process driving it. With the exception of dyke propagation during rifting, this effect has not been widely reported. However, it may occur at other volcanoes where active fault zones lie in close enough proximity to volcanic belts to allow interaction with magma reservoirs.

Acknowledgements

We thank all of the staff at the Instituto Geofisico in Quito Ecuador who have worked on monitoring the unrest at Chiles–Cerro Negro, including instrument deployment and maintenance, data processing and field observations. SKE is funded by a European Space Agency Living Planet Fellowship (IMRICA). SKE and JB were supported by STREVA (NERC grant number: NE/J020052/1) and SKE, JRE and JB also by the Centre for the Observations and Modelling of Earthquakes, Volcanoes and Tectonics (COMET). JRE was funded by EWF (NERC grant number: NE/J02001X/1_1) and LICS (NE/K011006/1). JMN is supported by the IRD-France in the framework of the International Joint Laboratory Earthquakes and Volcanoes in the Northern Andes. The IGEPN expresses thanks to UNAVCO for support in GPS instrumentation and to the SENPLADES Project for providing funding for instrumentation and logistical support. The Committee for Earth Observation Satellite Volcano Pilot project provided CosmoSkymed (ASI) and TerraSAR-X (DLR) imagery. RADARSAT-2 data were provided by the Canadian Space Agency. We thank Mario Ruiz, Rebecca Salvage, Stephen Hernandez and Rowena Lohman for very helpful conversations. This work forms part of the CEOS Volcano Pilot for Disaster Risk Reduction.

Appendix A. Supplementary material

Supplementary material related to this article can be found online at http://dx.doi.org/10.1016/j.epsl.2016.06.046.

References

Albino, F., Sigmundsson, F., 2014. Stress transfer between magma bodies: influence of intrusions prior to 2010 eruptions at Eyjafjallajökull volcano, Iceland. J. Geophys. Res., Solid Earth 119 (4), 2964–2975. http://dx.doi.org/10.1002/2013JB010510.

Altamimi, Z., Collilieux, X., Métivier, L., 2011. ITRF2008: an improved solution of the international terrestrial reference frame. J. Geod. 85 (8), 457–473. http://dx.doi.org/10.1007/s00190-011-0444-4.

Battaglia, J., Métaxian, J.P., Garaebiti, E., 2012. Earthquake–volcano interaction imaged by coda wave interferometry. Geophys. Res. Lett. 39 (11). http://dx.doi.org/10.1029/2012GL052003.

Beauval, C., Yepes, H., Bakun, W.H., Egred, J., Alvarado, A., Singaucho, J.C., 2010. Locations and magnitudes of historical earthquakes in the Sierra of Ecuador (1587–1996). Geophys. J. Int. 181 (3), 1613–1633. http://dx.doi.org/10.1111/j.1365-246X.2010.04569.x.

Benoit, J.P., McNutt, S.R., 1996. Global volcanic earthquake swarm database and preliminary analysis of volcanic earthquake swarm duration. Ann. Geophys. 39 (2). http://dx.doi.org/10.4401/ag-3963.

Bettinelli, P., Avouac, J.P., Flouzat, M., Bollinger, L., Ramillien, G., Rajaure, S., Sapkota, S., 2008. Seasonal variations of seismicity and geodetic strain in the Himalaya induced by surface hydrology. Earth Planet. Sci. Lett. 266 (3), 332–344. http://dx.doi.org/10.1016/j.epsl.2007.11.021.

Biggs, J., Amelung, F., Gourmelen, N., Dixon, T.H., Kim, S.W., 2009. InSAR observations of 2007 Tanzania rifting episode reveal mixed fault and dyke extension in an immature continental rift. Geophys. J. Int. 179 (1), 549–558. http://dx.doi.org/10.1111/j.1365-246X.2009.04262.x.

Biggs, J., Bastow, I.D., Keir, D., Lewi, E., 2011. Pulses of deformation reveal frequently recurring shallow magmatic activity beneath the Main Ethiopian Rift. Geochem. Geophys. Geosyst. 12 (9). http://dx.doi.org/10.1029/2011GC003662.

Biggs, J., Chivers, M., Hutchinson, M.C., 2013. Surface deformation and stress interactions during the 2007–2010 sequence of earthquake, dyke intrusion and eruption in northern Tanzania. Geophys. J. Int. 195 (1), 16–26. http://dx.doi.org/10.1093/gji/ggt226.

Chen, C.W., Zebker, H.A., 2002. Phase unwrapping for large SAR interferograms: statistical segmentation and generalized network models. IEEE Trans. Geosci. Remote Sens. 40 (8), 1709–1719. http://dx.doi.org/10.1109/TGRS.2002.802453.

Chouet, B.A., Matoza, R.S., 2013. A multi-decadal view of seismic methods for detecting precursors of magma movement and eruption. J. Volcanol. Geotherm. Res. 252, 108–175. http://dx.doi.org/10.1016/j.jvolgeores.2012.11.013.

Cortés, G.P., Calvache Velasco, M.L., 1997. Informe sobre la Evaluación de la Amenzana Volcánica del Chiles y Cerro Negro. República de Colombia Ministerio de Mina Y Energía, Instituto de investigaciones en Geociencias, Mineria y Química, Observatorio Vulcanológico y Sismologico de Pasto.

Diez, M., La Femina, P.C., Connor, C.B., Strauch, W., Tenorio, V., 2005. Evidence for static stress changes triggering the 1999 eruption of Cerro Negro Volcano, Nicaragua and regional aftershock sequences. Geophys. Res. Lett. 32 (4). http://dx.doi.org/10.1029/2004GL021788.

Ego, F., Sébrier, M., Lavenu, A., Yepes, H., Egues, A., 1996. Quaternary state of stress in the Northern Andes and the restraining bend model for the Ecuadorian Andes. Tectonophysics 259 (1), 101–116. http://dx.doi.org/10.1016/0040-1951(95)00075-5.

Elliott, J.R., Walters, R.J., England, P.C., Jackson, J.A., Li, Z., Parsons, B., 2010. Extension on the Tibetan plateau: recent normal faulting measured by InSAR and body wave seismology. Geophys. J. Int. 183 (2), 503–535. http://dx.doi.org/10.1111/j.1365-246X.2010.04754.x.

Funning, G.J., Parsons, B., Wright, T.J., Jackson, J.A., Fielding, E.J., 2005. Surface displacements and source parameters of the 2003 Bam (Iran) earthquake from ENVISAT advanced synthetic aperture radar imagery. J. Geophys. Res. 110 (B9), B09406. http://dx.doi.org/10.1029/2004JB003338.

Hanssen, R.F., 2001. Radar Interferometry: Data Interpretation and Error Analysis, vol. 2. Springer Science and Business Media.

Hill, D.P., 2006. Unrest Long Valley Caldera, California, 1978–2004. Geol. Soc. (Lond.) Spec. Publ. 269 (1), 1–24. http://dx.doi.org/10.1144/GSL.SP.2006.269.01.02.

Instituto Geofisico Escuela Nacional Politecnica, 2014. Informe del volcán Chiles–Cerro Negro. www.igepn.edu.ec/chiles-cerro-negro/informes-chiles-cerro-negro/ccn-especiales.

Jay, J.A., Delgado, F.J., Torres, J.L., Pritchard, M.E., Macedo, O., Aguilar, V., 2015. Deformation and seismicity near Sabancaya volcano, southern Peru, from 2002 to 2015. Geophys. Res. Lett. 42 (8), 2780–2788. http://dx.doi.org/10.1002/2015GL063589.

Jolly, A.D., McNutt, S.R., 1999. Seismicity at the volcanoes of Katmai National Park, Alaska, July 1995–December 1997. J. Volcanol. Geotherm. Res. 93 (3), 173–190. http://dx.doi.org/10.1016/S0377-0273(99)00115-8.

Jónsson, S., 2009. Stress interaction between magma accumulation and trapdoor faulting on Sierra Negra volcano Galápagos. Tectonophysics 471 (1), 36–44. http://dx.doi.org/10.1016/j.tecto.2008.08.005.

King, R.W., Bock, Y., 1999. Documentation for the GAMIT GPS Analysis Software. Mass. Inst. of Technol., Cambridge, Mass.

Lin, J., Stein, R.S., 2004. Stress triggering in thrust and subduction earthquakes and stress interaction between the southern San Andreas and nearby thrust and strike-slip faults. J. Geophys. Res., Solid Earth (1978–2012) 109 (B2). http://dx.doi.org/10.1029/2003JB002607.

Linde, A.T., Sacks, I.S., 1998. Triggering of volcanic eruptions. Nature 395 (6705), 888–890. http://dx.doi.org/10.1038/27650.

Lu, Z., Dzurisin, D., 2014. InSAR Imaging of Aleutian Volcanoes: Monitoring a Volcanic Arc from Space. Springer Science and Business Mediahttp://dx.doi.org/10.1007/978-3-642-00348-6_6]10.1007/978-3-642-00348-6_6 .

Lundgren, P., Samsonov, S.V., López Velez, C.M., Ordoñez, M., 2015. Deep source model for Nevado del Ruiz Volcano, Colombia, constrained by Interferometric Synthetic Aperture Radar observations. Geophys. Res. Lett. 42 (12), 4816–4823. http://dx.doi.org/10.1002/2015GL063858.

Maccaferri, F., Rivalta, E., Passarelli, L., Aoki, Y., 2016. On the mechanisms governing dike arrest: insight from the 2000 Miyakejima dike injection. Earth Planet. Sci. Lett. 434, 64–74. http://dx.doi.org/10.1016/j.epsl.2015.11.024.

Manga, M., Brodsky, E., 2006. Seismic triggering of eruptions in the far field: volcanoes and geysers. Annu. Rev. Earth Planet. Sci. 34, 263–291. http://dx.doi.org/10.1146/annurev.earth.34.031405.125125.

Moran, S., Stihler, S., Power, J., 2002. A tectonic earthquake sequence preceding the April–May 1999 eruption of Shishaldin Volcano, Alaska. Bull. Volcanol. 64 (8), 520–524. http://dx.doi.org/10.1007/s00445-002-0226-1.

Moran, S.C., Newhall, C., Roman, D.C., 2011. Failed magmatic eruptions: late-stage cessation of magma ascent. Bull. Volcanol. 73 (2), 115–122. http://dx.doi.org/10.1007/s00445-010-0444-x.

Mothes, P.A., Nocquet, J.M., Jarrín, P., 2013. Continuous GPS network operating throughout Ecuador. Eos, Trans. Am. Geophys. Union 94 (26), 229–231. http://dx.doi.org/10.1002/2013EO260002.

Nishimura, T., Fujiwara, S., Murakami, M., Tobita, M., Nakagawa, H., Sagiya, T., Tada, T., 2001. The M6.1 earthquake triggered by volcanic inflation of Iwate volcano, northern Japan, observed by satellite radar interferometry. Geophys. Res. Lett. 28 (4), 635–638. http://dx.doi.org/10.1029/2000GL012022.

Nocquet, J.M., Villegas-Lanza, J.C., Chlieh, M., Mothes, P.A., Rolandone, F., Jarrin, P., Cisneros, D., Alvarado, A., Audin, L., Bondoux, F., Martin, X., Font, Y., Régnier, M., Vallée, M., Tran, T., Beauval, C., Maguiña Mendoza, J.M., Martinez, W., Tavera, H., Yepes, H., 2014. Motion of continental slivers and creeping subduction in the Northern Andes. Nat. Geosci. 7 (4), 287–291. http://dx.doi.org/10.1038/NGEO2099.

Okada, Y., 1985. Surface deformation due to shear and tensile faults in a half-space. Bull. Seismol. Soc. Am. 75 (4), 1135–1154.

Passarelli, L., Maccaferri, F., Rivalta, E., Dahm, T., Boku, E.A., 2013. A probabilistic approach for the classification of earthquakes as 'triggered' or 'not triggered'. J. Seismol. 17 (1), 165–187. http://dx.doi.org/10.1007/s10950-012-9289-4.

Pritchard, M.E., Jay, J.A., Aron, F., Henderson, S.T., Lara, L.E., 2013. Subsidence at southern Andes volcanoes induced by the 2010 Maule, Chile earthquake. Nat. Geosci. 6 (8), 632–636. http://dx.doi.org/10.1038/ngeo1855.

Pritchard, M.E., Simons, M., 2004. An InSAR-based survey of volcanic deformation in the central Andes. Geochem. Geophys. Geosyst. 5 (2). http://dx.doi.org/10.1029/2003GC000610.

Riel, B., Milillo, P., Simons, M., Lundgren, P., Kanamori, H., Samsonov, S., 2015. The collapse of Bárðarbunga caldera, Iceland. Geophys. J. Int. 202 (1), 446–453. http://dx.doi.org/10.1093/gji/ggv157.

Roman, D.C., Power, J.A., 2011. Mechanism of the 1996–97 non-eruptive volcano-tectonic earthquake swarm at Iliamna Volcano, Alaska. Bull. Volcanol. 73 (2), 143–153. http://dx.doi.org/10.1007/s00445-010-0439-7.

Rosen, P., Eineder, M., Rabus, B., Gurrola, E., Hensley, S., Knoepfle, W., Breit, H., Roth, A., Werner, M., 2001. SRTM-mission-cross comparison of X and C band data properties. In: Geoscience and Remote Sensing Symposium, 2001, IGARSS'01, IEEE 2001 International, vol. 2. IEEE, pp. 751–753.

Rosen, P., Lavalle, M., Pi, X., Buckley, S., Szeliga, W., Zebker, H., Gurrola, E., 2011. Techniques and tools for estimating ionospheric effects in interferometric and polarimetric SAR data. In: Geoscience and Remote Sensing Symposium (IGARSS), 2011 IEEE International. IEEE, pp. 1501–1504.

Rubinstein, J.L., La Rocca, M., Vidale, J.E., Creager, K.C., Wech, A.G., 2008. Tidal modulation of nonvolcanic tremor. Science 319 (5860), 186–189. http://dx.doi.org/10.1126/science.1150558.

Ruiz, G., Cordova, A., Ruiz, M., Alvarado, A., 2013. Informe Tecnico de los Volcanes Cerro Negro y Chiles. Technical report, IG-EPN.

Salvage, R., 2015. Using seismic signals to forecast volcanic processes. PhD Thesis. Univeristy of Leeds.

SGC, 2014. Boletín Mensual No. 04-2014 – Periodo evaluado: Abril de 2014. Servicio Geológico Colombiano, Observatorio Vulcanológico y Sismológico de Pasto (OCSP). http://www2.sgc.gov.co/Pasto/Publicaciones/Reportes-de-actividad/Reportes-Mensuales—Boletines-Informativos/2014.aspx.

Shuler, A., Nettles, M., Ekström, G., 2013. Global observation of vertical-CLVD earthquakes at active volcanoes. J. Geophys. Res., Solid Earth 118 (1), 138–164. http://dx.doi.org/10.1029/2012JB009721.

Stein, R.S., 1999. The role of stress transfer in earthquake occurrence. Nature 402 (6762), 605–609. http://dx.doi.org/10.1038/45144.

Takada, Y., Fukushima, Y., 2013. Volcanic subsidence triggered by the 2011 Tohoku earthquake in Japan. Nat. Geosci. 6 (8), 637–641. http://dx.doi.org/10.1038/ngeo1857.

Toda, S., Stein, R.S., Sagiya, T., 2002. Evidence from the AD 2000 Izu islands earthquake swarm that stressing rate governs seismicity. Nature 419 (6902), 58–61. http://dx.doi.org/10.1038/nature00997.

Vallée, M., Charléty, J., Ferreira, A.M.G., Delouis, B., Vergoz, J., 2011. SCARDEC: a new technique for the rapid determination of seismic moment magnitude, focal mechanism and source time functions for large earthquakes using body wave deconvolution. Geophys. J. Int. 184, 338–358. http://dx.doi.org/10.1111/j.1365-246X.2010.04836.x.

Vidale, J.E., Boyle, K.L., Shearer, P.M., 2006. Crustal earthquake bursts in California and Japan: their patterns and relation to volcanoes. Geophys. Res. Lett. 33 (20). http://dx.doi.org/10.1029/2006GL027723.

Wegmuller, U., Werner, C., Strozzi, T., 1998. July. SAR interferometric and differential interferometric processing chain. In: International Geoscience And Remote Sensing Symposium, vol. 2. Institute Of Electrical and Electronicsengineers, Inc. (IEE), pp. 1106–1108.

White, R., McCausland, W., 2016. Volcano-tectonic earthquakes: a new tool for estimating intrusive volumes and forecasting eruptions. J. Volcanol. Geotherm. Res. 309, 139–155. http://dx.doi.org/10.1016/j.jvolgeores.2015.10.020.

Wicks, C.W., Thatcher, W., Dzurisin, D., Svarc, J., 2006. Uplift, thermal unrest and magma intrusion at Yellowstone caldera. Nature 440 (7080), 72–75. http://dx.doi.org/10.1038/nature04507.

Wicks, C., de La Llera, J.C., Lara, L.E., Lowenstern, J., 2011. The role of dyking and fault control in the rapid onset of eruption at Chaitén volcano, Chile. Nature 478 (7369), 374–377. http://dx.doi.org/10.1038/nature10541.

Wright, T.J., Ebinger, C., Biggs, J., Ayele, A., Yirgu, G., Keir, D., Stork, A., 2006. Magma-maintained rift segmentation at continental rupture in the 2005 Afar dyking episode. Nature 442 (7100), 291–294. http://dx.doi.org/10.1038/nature04978.

Xu, W., Jónsson, S., Corbi, F., Rivalta, E., 2016. Graben formation and dike arrest during the 2009 Harrat Lunayyir dike intrusion in Saudi Arabia: insights from InSAR, stress calculations and analog experiments. J. Geophys. Res. 121 (4), 2837–2851. http://dx.doi.org/10.1002/2015JB012505.

Yang, X.M., Davis, P.M., Dieterich, J.H., 1988. Deformation from inflation of a dipping finite prolate spheroid in an elastic half-space as a model for volcanic stressing. J. Geophys. Res., Solid Earth 93 (B5), 4249–4257. http://dx.doi.org/10.1029/JB093iB05p04249.

Yokoyama, I., 2001. The largest magnitudes of earthquakes associated with some historical volcanic eruptions and their volcanological significance. Ann. Geofis. 44 (5/6). http://dx.doi.org/10.4401/ag-3553.